Circuit-Based Magnetic Hyperbolic Cavities

Yuqian Wang, Zhiwei Guo⬤,[*] Youqi Chen, Xu Chen, Haitao Jiang⬤, and Hong Chen[†]

Key Laboratory of Advanced Micro-structure Materials, MOE, School of Physics Science and Engineering,
Tongji University, Shanghai 200092, China

Optical resonant cavities play an important role in electromagnetic wave control; they can confine electromagnetic waves and improve the interaction between light and matter. However, because of the limitations of the standing-wave formation conditions for Fabry-Perot-type resonance, the miniaturization of optical resonant cavities formed using traditional materials is difficult. Recently, the miniaturization of three-dimensional optical resonant cavities has been demonstrated based on electric hyperbolic metamaterials (HMMs); their isofrequency contour takes the form of an open hyperboloid because the principal components of the permittivity tensor have opposite signs. Here, based on the permeability tensor, we propose theoretically and verify experimentally a planar magnetic hyperbolic cavity with a subwavelength scale, $(\lambda/12) \times (\lambda/17)$, using a circuit-based HMM in the microwave regime. Furthermore, the anomalous scaling laws in the circuit-based magnetic hyperbolic cavities are studied. As the frequency increases, the mode order decreases, which is markedly different from traditional cavities. It is also possible to realize size-independent cavity modes based on the HMMs by design. In addition, by considering a composite structure that contains two hyperbolic cavities, the coupling of two hyperbolic cavity modes in the near-field regime is demonstrated. The circuit-based hyperbolic cavities not only extend previous research work on hyperbolic cavities to magnetic HMMs, but they also have a planar structure that is easier to integrate and has a smaller loss. Finally, the hyperbolic cavities may enable their use in some microwave-related applications, such as in high-sensitivity sensors, resonance imaging, and miniaturized narrowband filters.

I. INTRODUCTION

Advances in the fields of hyperbolic metamaterials (HMMs) have greatly improved the ability to control electromagnetic waves in previously inaccessible ways [1–6]. By using the abnormal dispersion property of HMMs, flexible control of the propagation of electromagnetic waves is realized, such as negative refraction [7–9], collimation [10,11], beam splitting [12–14], and anomalous scattering [15,16]. Importantly, HMMs support propagating high-k modes and possess an enhanced photonic density of states [17,18], leading to promising applications that include hyperlenses that can overcome diffraction limits [19–21], sensors [22,23], the giant Unruh effect [24], fingerprinting [25], and long-range energy transfer [26–30]. It is well known that the isofrequency contour (IFC) of normal materials (such as air) is a closed sphere, where the allowed wave vectors are limited. However, the IFC of HMMs forms an open hyperbolic curve that allows propagating waves with large wave vectors. The mismatch between the high-k modes in HMMs and the modes with limited wave

vectors in the surrounding medium lead to total internal reflections. Therefore, HMMs with high-k modes can also be used to design high-performance optical devices, such as waveguides with high confinement [26–33] and resonant cavities with a high quality factor and a small modal volume [34–37].

Hyperbolic cavities have attracted considerable interest because of their anomalous scaling laws (ASLs), where a high-order resonance mode corresponds to a lower frequency, and cavities with different sizes can resonate at the same frequency and the same mode order [34–37]. ASLs have also been studied because of the abnormal whispering-gallery modes in HMM cavities with spherical [38,39] and tubular geometry [40]. In particular, hyperbolic cavities with an ultrasmall size can greatly enhance light-matter interactions, including increasing the rates of spontaneous emission [37,39,41,42], which may be useful in the field of cavity quantum electrodynamics and lasers [43–45]. However, there are some aspects of hyperbolic cavities that should be noted. (1) To date, nearly all hyperbolic cavities use hyperbolic dispersion caused by an electric response, which restricts the functionality of the hyperbolic cavity to transverse-magnetic (TM) polarized waves with an electric field parallel to the optical axis in the principal plane. To overcome this limitation

and extend their application to transverse-electric (TE) polarized waves, magnetic HMMs (the principal components of its permeability tensor have opposite signs) [46] are needed to construct magnetic hyperbolic cavities. (2) Hyperbolic cavities have been studied based on three-dimensional (3D) structures using dielectric/metal multilayered structures [35] and nanowire structures [34]. Along with the development of planar HMMs in recent years [47–53], the study of planar hyperbolic cavities may be easier to integrate and have a smaller loss. (3) Resonant hyperbolic cavities can be seen as meta-atoms, which may play an important role in classical analog quantum optical phenomena, such as HMM-assisted electromagnetic induced transparency (EIT) [30] and Fano resonance [54,55]. Therefore, the near-field coupling between surface waves at the resonant hyperbolic metasurface is also a very interesting topic of research [47,48].

Transmission lines (TLs) with lumped elements can realize various electromagnetic parameters [56,57]. Specifically, HMMs can be well constructed using circuit-based metamaterials in the microwave regime [58–62]. So far, circuit-based HMMs have been widely used to study many interesting phenomena, such as crosslike emission [58], topological transition of the IFC [59], and the photonic spin Hall effect [60]. Here, by using two-dimensional (2D) TLs with lumped elements, circuit-based magnetic hyperbolic cavities are designed and fabricated with subwavelength-scale properties and planarization. Based on the near-field detection method, we demonstrate the ASLs in the circuit-based hyperbolic cavities. Furthermore, a study of the coupling between two hyperbolic cavities is presented, which is particularly relevant for classical EIT and Fano resonance based on metamaterials. Our findings not only present a type of hyperbolic cavity with ASLs, but are also very useful for a variety of applications in planar integrated photonics, including for sensors, detectors, and switches.

This work is organized as follows: Sec. II covers the design of the circuit-based magnetic hyperbolic cavity; in Sec. III, the physical mechanism of the ASLs in the 2D optical resonant cavity is analyzed, and both simulations and experiments are carried out to verify the anomalous scaling laws; in Sec. IV, the coupling between two hyperbolic cavities is studied, and destructive interference and a tunable quality factor for the hyperbolic cavity modes can be realized. Finally, Sec. V summarizes the conclusions of this work.

II. PLANAR MAGNETIC HYPERBOLIC CAVITY REALIZED USING CIRCUIT-BASED METAMATERIALS

Circuit-based magnetic HMMs are designed by loading lumped elements into the 2D TLs, as shown in Fig. 1. Here, the hyperbolic cavity is marked by the purple dashed line and the outside region is the circuit-based background medium. The structure is constructed on a commercial printed circuit board, F4B (relative permittivity $\varepsilon_r = 2.2$ and loss tangent $\tan \delta = 0.0079$), with a thickness of $h = 1.6$ mm. The width of the microstrip is $w = 2.8$ mm and the length of a unit cell is $p = 12$ mm. The dimensions of the structure in the x and z directions are 172.4 and 123.6 mm, respectively. In the proposed structure, the effective HMM is realized by loading series lumped capacitors of $C = 5$ pF in the x direction, and no capacitors are loaded in the background medium.

The effective circuit models of the HMM and background medium are shown in Fig. 2(a). The structural factor of the TL is defined as $g = Z_0/\eta_{\text{eff}}$, where Z_0 and η_{eff} are the characteristic impedance and effective wave impedance of the TL, respectively [63–65]. The structure factor of the designed structure is $g \approx 0.255$ [12]. Because the unit size in the TL system is much smaller than that of the wavelength, the effective permittivity of the 2D TLs
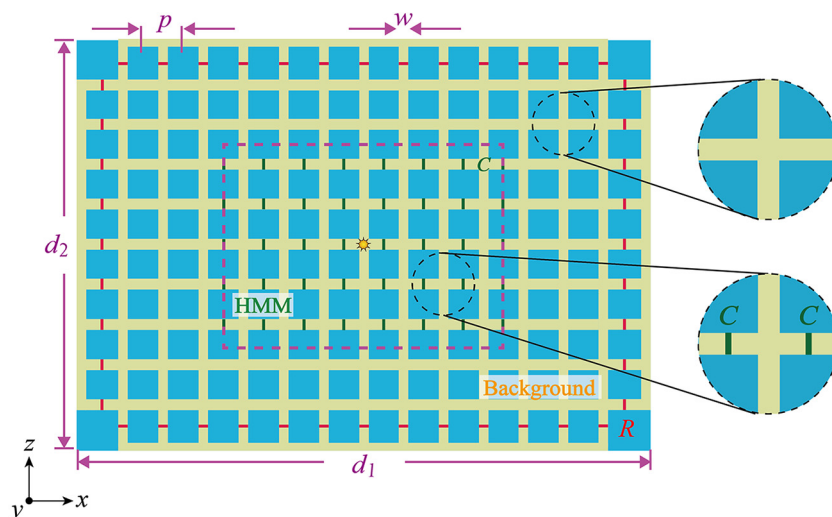

FIG. 1. Schematic of the TL-based structure, in which the HMM is embedded in the background region. $d_1 = 172.4$ mm, $d_2 = 123.6$ mm, $p = 12$ mm, $w = 2.8$ mm, $C = 5$ pF, and $R = 71.4$ Ω. Unit structures of HMM and background medium are enlarged on the right.
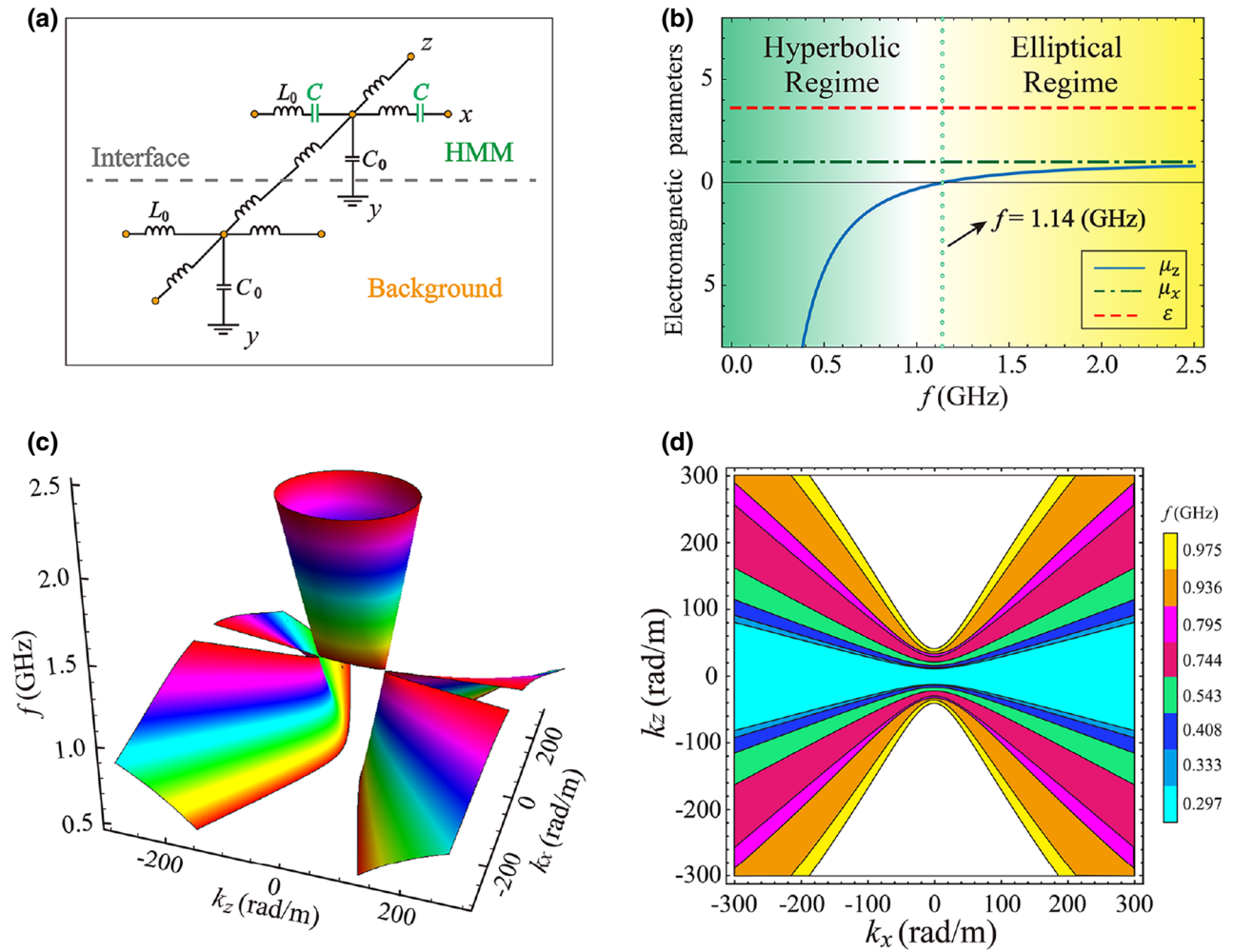
FIG. 2. (a) 2D circuit models of the HMM and background medium. (b) Effective anisotropic electromagnetic parameters based on TL when capacitors are loaded in the x direction. (c) 3D dispersion relationships of the TL-based metamaterials with the loaded series lumped capacitors. (d) Cross graphs of the 3D dispersion relationships for some frequencies in (c).

for a quasistatic TE polarized solution can be written as [10–12]

$$\varepsilon = 2C_0 g/\varepsilon_0, \quad \mu_x = \frac{L_0}{g\mu_0},$$
$$\mu_z = \frac{L_0}{g\mu_0} - \frac{1}{\omega^2 C d g \mu_0},$$ (1)

where ε_0 and μ_0 are the permittivity and permeability of vacuum, respectively; ω is the angular frequency; and C_0 and L_0 denote the per-unit length capacitance and inductance of the TL, respectively [10–12]. From Eq. (1), $\varepsilon \approx 3.63$ (red dashed line), $\mu_x = 1$ (green dot dash line), and the dependence of μ_z on the frequency (blue solid line) are drawn in Fig. 2(b). By tuning the sign of μ_z from positive to negative, a topological transition of the IFC from closed elliptical to open hyperbolic dispersion can be generated. The gradient color from green to yellow in Fig. 2(b) corresponds to the regime from hyperbolic to elliptical. Notably, this change is a topological transition and

it is described as the metric signature transition [17]. In particular, $\mu_z \approx 0$, when the frequency is 1.14 GHz, which is marked by the green dotted line. When the frequency is smaller than this critical value, μ_z has a negative value. The dispersion relation of the circuit-based metamaterials is described by [10–12]

$$\frac{k_x^2}{\varepsilon \mu_z} + \frac{k_z^2}{\varepsilon \mu_x} = \left(\frac{\omega}{c}\right)^2,$$ (2)

where k_x and k_z are the x and z components of the wave vector, respectively, and c is the speed of light in vacuum.

Based on Eq. (2), we calculate the 3D dispersion relationship of the 2D TL with lumped capacitors in the x direction, as shown in Fig. 2(c). A topological transition of an IFC from an elliptical dispersion to a hyperbolic dispersion is produced by varying the frequency. The critical phase ($f = 1.14$ GHz) of this topological transition corresponds to an anisotropic mu-near-zero material. Here,
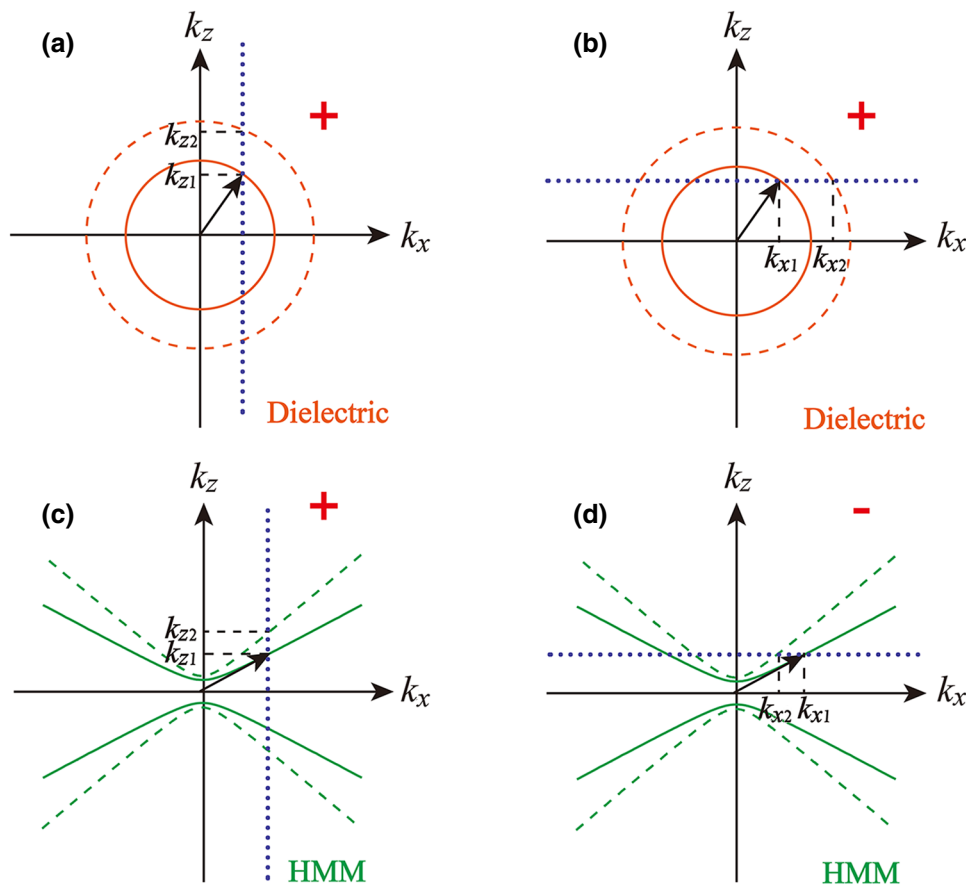
FIG. 3. IFCs for the dielectric (a),(b) and HMM (c),(d), where the solid and dashed lines correspond to the values at frequencies ω and $\omega + \delta\omega$, respectively. Dotted line in each graph is used to represent the determined k_x or k_z.

we focus on the hyperbolic dispersion, so only the cases with a frequency lower than 1.14 GHz are considered, and the HMMs realized by the TL have wide-band characteristics. Eight different IFCs of the HMMs are used as examples, as given in Fig. 2(d). It can be seen that as the frequency increases, the opening angle of the hyperbola along the z direction becomes smaller and smaller. The background medium realized by the circuit-based structure is an isotropic medium ($\varepsilon \approx 3.63$, $\mu = 1$), with an IFC corresponding to a closed circle [6]. The mode mismatch between the HMM and the background medium causes the inner HMM to function as a planar magnetic hyperbolic cavity.

At the end of this section, we illustrate the analogy between wave propagation in a homogeneous 3D HMM and that in its 2D circuit-based counterpart. It is clear that the cross-section surface of a hyperboloid is a hyperbola [6]. Therefore, a homogeneous 3D HMM can be extended to its 2D circuit-based counterpart, when the wave propagates in a special plane. As an example, the similarity between electromagnetic wave propagation in a 2D circuit-based HMM [12] and that in a 3D structure [14] is demonstrated. However, it should be noted that the bulk-wave propagation in the homogeneous 3D HMM and surface-mode propagation along the 2D circuit-based HMM can differ significantly. In the homogeneous 3D

HMM, the bulk wave can only propagate within a certain range of angles, and the field perpendicular to the hyperbolic asymptotes is much stronger than that elsewhere because of the larger optical density of states [60]. However, the excitation and propagation of the surface mode in 2D circuit-based HMMs is constrained by the boundary conditions, and the field strength decreases exponentially in the direction perpendicular to the interface. Specifically, the 2D circuit-based HMMs are demonstrated to realize interesting hybrid TE-TM polarization surface waves [62].

III. SIMULATION AND EXPERIMENTAL VERIFICATION OF THE ABNORMAL SCALING LAW

The ASL of the 2D hyperbolic cavity can be explained very well by the IFCs. For a traditional cavity made of a dielectric, the corresponding IFC is a closed circle, which can be seen in Figs. 3(a) and 3(b). The dashed lines denote the IFC at a frequency slightly above the frequency of the solid lines. In this medium, when the wave vector in the x direction is fixed (marked by a blue dotted line along the z direction), the wave vector at a higher frequency is larger than one at a lower frequency, $k_{z2} > k_{z1}$, as shown in Fig. 3(a). Because the dielectric is isotropic, when the wave vector in the z direction is fixed (which is marked by

a blue dotted line along the x direction), the wave vector in the x direction similarly meets $k_{x2} > k_{x1}$, as shown in Fig. 3(b). Therefore, both the wave vectors in the x and z directions increase as the frequency increases for the dielectric. The wave-vector property for the anisotropic HMM is clearly different for the two different directions. In the HMM, when the wave vector in the x direction is fixed, the wave vector at a higher frequency is larger than that at lower frequency ($k_{z2} > k_{z1}$) in Fig. 3(c), which is similar to the dielectric in Fig. 3(a). However, when the wave vector in the z direction is fixed, the wave vector in the x direction meets $k_{x2} < k_{x1}$, as shown in Fig. 3(d). Therefore, in the HMM, the wave vectors in the z and x directions increase as the frequency increases and decrease as the frequency decreases, respectively. In other words, the normal and abnormal scaling laws are applicable to the z and x directions in the HMMs, respectively. The normal and abnormal properties of the wave vectors are marked by a "+" and "−," respectively, in Fig. 3.

To demonstrate the abnormal scaling law in the HMM, using the commercial software package (CST Microwave Studio), the hyperbolic cavity modes are excited by a current source close to the center of the structure. In the simulation, the perfect matching boundary condition is used [63–65]. The response of the system is probed in the vicinity of the structure surface in Fig. 4. The simulated out-of-plane electric field E_y spectrum is probed at the center of the cavity and then it is plotted as a function of the frequency. In the simulated E_y spectra, the cavity modes with high electromagnetic confinement can be clearly identified. From Fig. 4, it can be found that there are 11 peaks within a certain frequency range. In particular, eight cavity modes are marked, according to the mode order in Fig. 4, and these modes will be used to demonstrate the anisotropic scaling law for the circuit-based hyperbolic cavity. These cavity modes are labeled as
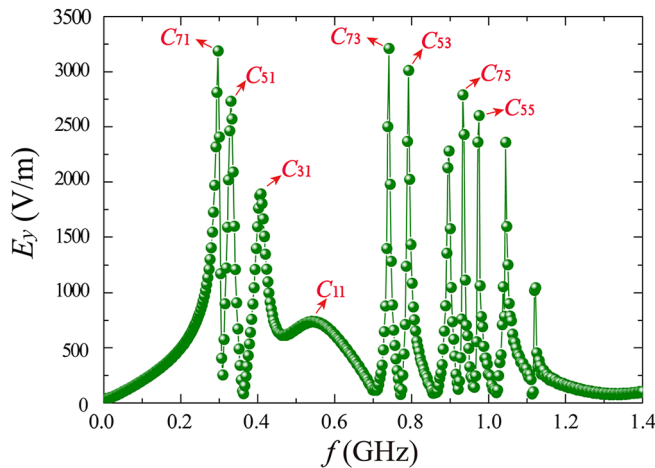

FIG. 4.   Simulated E_y spectra for the hyperbolic cavity modes. Eight modes are marked by different order numbers.

C_{mn}, where m and n represent the order of multipolar resonances along the x direction and z direction, respectively [66].

First, the ASL of the circuit-based magnetic hyperbolic cavity is studied along the x direction. In Fig. 4, we first consider four cavity modes that are marked by red arrows and the corresponding order numbers are labeled C_{71}, C_{51}, C_{31}, and C_{11}. The electric field E_y distributions of these modes are shown in Fig. 5; here, it can clearly be seen that the higher-order mode is found at a lower resonant frequency in the hyperbolic cavity. The hyperbolic cavity is marked by the pink dashed line. For example, the frequency of the high-order mode C_{71} is 0.297 GHz, while the frequency of the low-order mode C_{11} is 0.543 GHz. By comparing modes C_{71}, C_{51}, C_{31}, and C_{11}, the anomalous property of the HMM mode order in the x direction is demonstrated. Moreover, the confinement strength of the different cavity modes can be clearly observed from the evanescent fields that extend outside the hyperbolic cavity in Fig. 5. The higher order mode has a stronger confined capacity, which is consistent with the spectrum in Fig. 4.

To further explain this phenomenon, the cases for orders three and five in the z direction are also studied in Fig. 6. Considering order three in the z direction and comparing Figs. 6(a) and 6(b), we find that the order of the hyperbolic cavity mode decreases with increasing frequency in the x direction. Similarly, for order five in the z direction, this abnormal scaling law is still observed when comparing Figs. 6(c) and 6(d). Therefore, the abnormal scaling law in the x direction of the hyperbolic cavity is fully demonstrated by three different orders (1, 3, and 5) in the z direction. Moreover, by considering the same mode order in the x direction, the mode order related to frequency in the z direction can be studied. By comparing Figs. 5(a), 6(a), and 6(c), we find that, for the same order in the x direction, the order of the hyperbolic cavity mode increases with increasing frequency in the z direction. For example, the frequency of the high-order mode is 0.297 GHz, while the frequencies of the low-order modes C_{71} and is 0.297 GHz, while the frequencies of the low-order modes C_{73} and C_{15} are 0.744 and 0.936 GHz, respectively. Therefore, the anisotropy of the hyperbolic cavity mode and the scaling laws in the x and z directions are anomalous and normal, respectively.

Next, the dependence of the hyperbolic cavity mode on the structure size is studied. The size of the hyperbolic cavity is identified by the number of unit cells in the x and z directions. Two cavities with different sizes are taken as examples and are characterized by $N_x = 7$, $N_z = 5$ and $N_x = 4$, $N_z = 4$ in Figs. 7(a) and 7(b), respectively. The influence of shortening the length of the hyperbolic cavity in the x and z directions on the cavity mode is then considered. First, the length in the z direction is fixed at $N_z = 5$, and the E_y spectra for the two cavities with $N_x = 5$ and $N_x = 7$ are shown in Fig. 7(c). The cavity modes C_{11} in
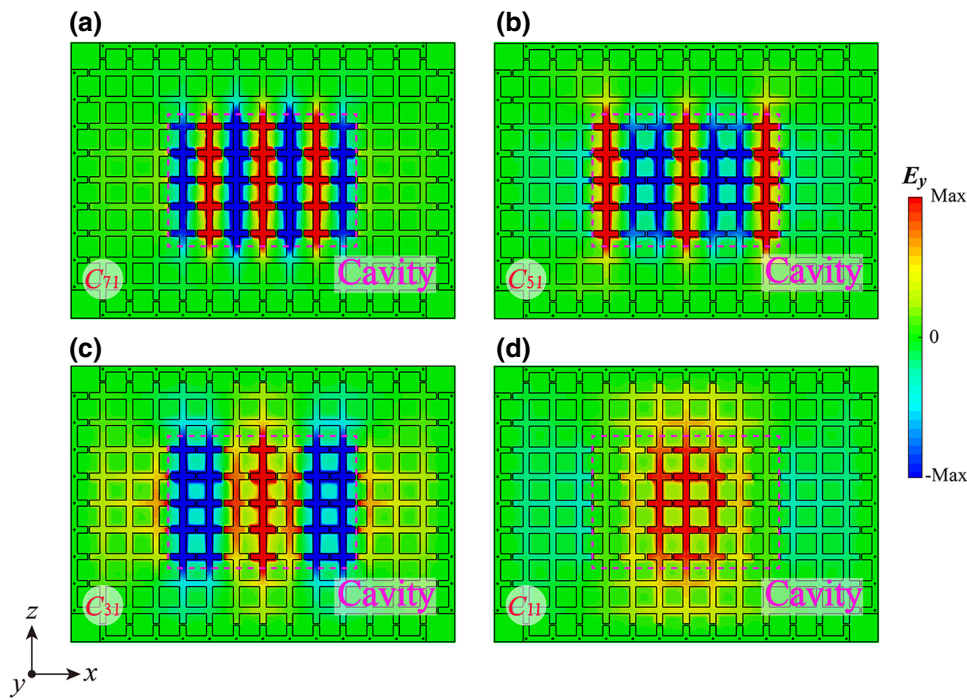
FIG. 5. Simulated near-field distributions of E_y at four different frequencies: (a) 0.297 GHz (order C_{11}), (b) 0.333 GHz (order C_{71}), (c) 0.408 GHz (order C_{31}), and (d) 0.543 GHz (order C_{11}). Order number for each case is shown at the lower left of each figure.

the two cavities are marked by red circles for visualization. From Fig. 7(c), it can be seen that the frequency of mode C_{11} blueshifts with decreasing length in the x direction. Next, the length in the x direction is fixed at $N_x = 7$, and the E_y spectra for the three cavities with $N_z = 1$, $N_z = 3$, and $N_z = 5$ are shown in Fig. 7(d). From Fig. 7(d), it can be seen that the frequency of mode C_{11} redshifts with decreasing length in the z direction. By comparing Figs. 7(c) and

7(d), we find that the dependence of the frequency of mode C_{11} on the structure's size is opposite to that in the x and z directions. Therefore, for hyperbolic cavities with different size combinations (including in the x and z directions), identical optical modes with the same resonant frequency and the same mode order can be realized with the proper design. Figure 7(e) shows this ASL of the hyperbolic cavity for the different structure sizes. While the size of the
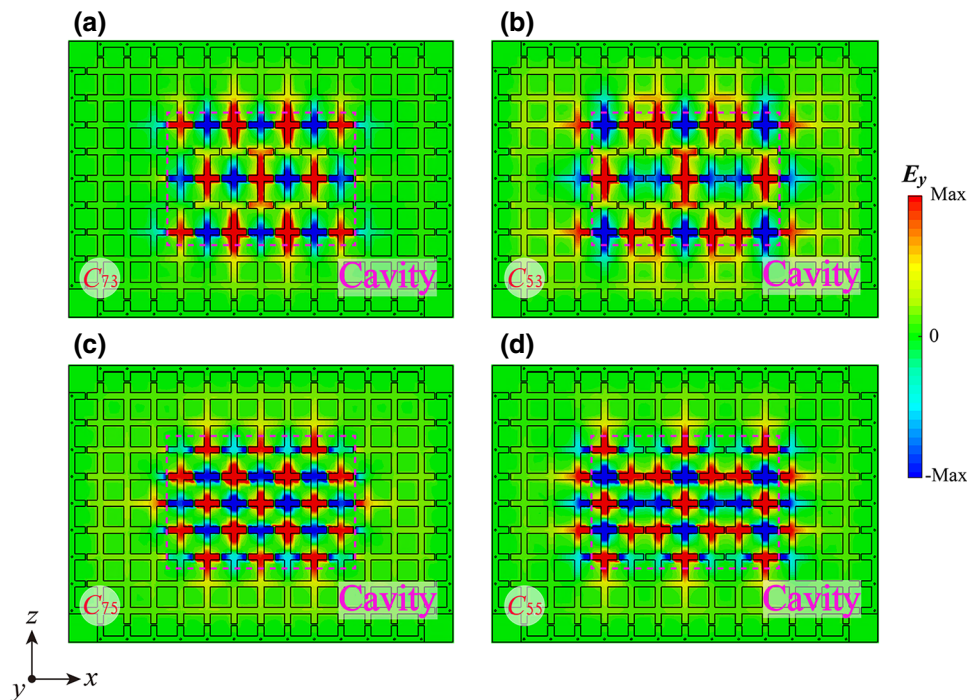

FIG. 6. Simulated near-field distributions of E_y at four different frequencies: (a) 0.744 GHz (order C_{73}), (b) 0.795 GHz (order C_{53}), (c) 0.936 GHz (order C_{75}), (d) 0.975 GHz (order C_{55}). The order number for each case is shown at lower left of each part.
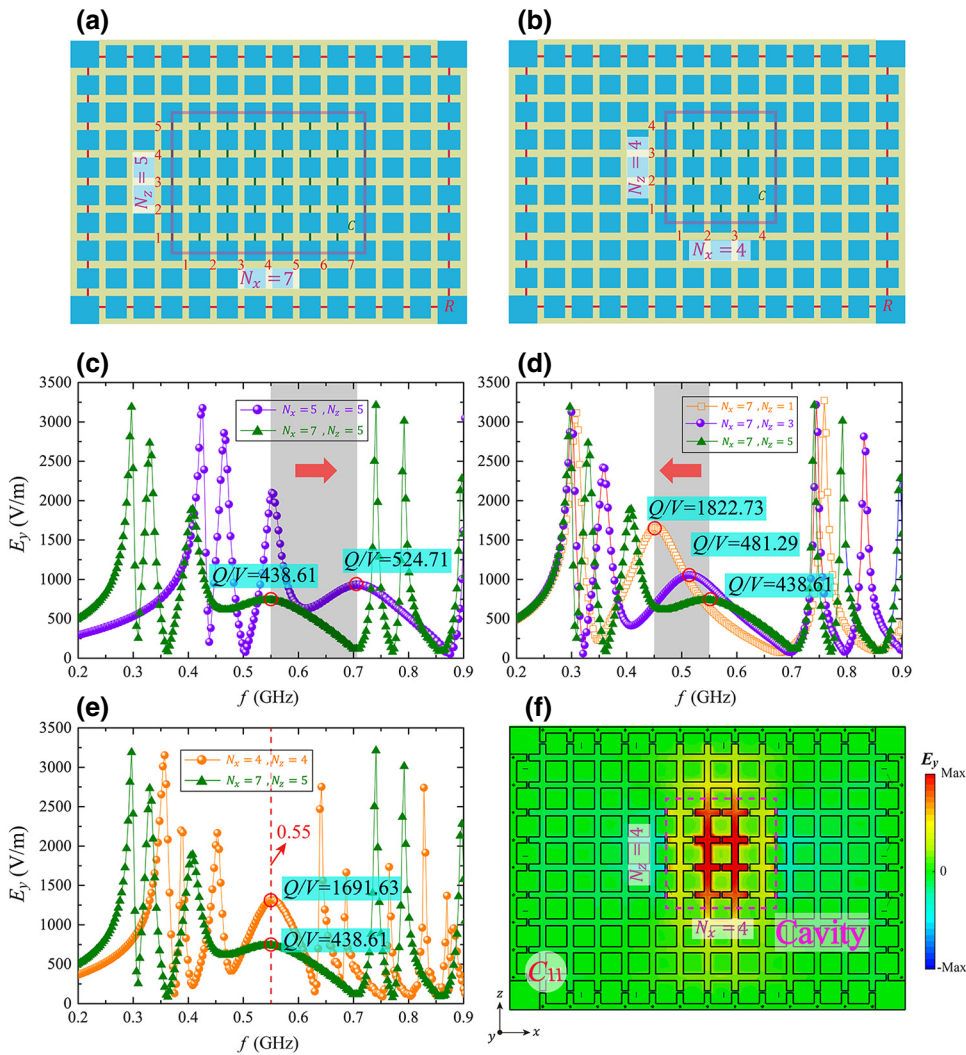
FIG. 7. Schematic of the TL-based structure with hyperbolic cavities of different sizes: (a) $N_x = 7$, $N_z = 5$, (b) $N_x = 4$, $N_z = 4$. (c) Simulated E_y spectra for the hyperbolic cavities with different N_x, and the cavity modes blueshift with decreasing N_x. (d) Similar to (c), but for different N_z, and the cavity modes red-shift with decreasing N_z. (e) Simulated E_y spectra for $N_x = 4$, $N_z = 4$ and the frequency of the C_{11} mode is the same as that of the C_{11} mode in the hyperbolic cavity with $N_x = 7$, $N_z = 5$. (f) Simulated near-field distribution of E_y at 0.55 GHz (order number C_{11}), for $N_x = 4$, $N_z = 4$.

cavity with $N_x = 7$, $N_z = 5$ is significantly larger than that of the cavity with $N_x = 4$, $N_z = 4$, the frequency of mode C_{11} is the same for both cavities. The fixed frequency (0.55 GHz) of mode C_{11} is marked by the red arrow in Fig. 7(e). The corresponding electric field E_y distribution for the cavity with $N_x = 4$, $N_z = 4$ is shown in Fig. 7(f) and is very similar to the cavity with $N_x = 7$, $N_z = 5$ in Fig. 5(d) at the same frequency. In particular, for the hyperbolic cavity mode C_{71} in the cavities with $N_x = 4$, $N_z = 4$ and $N_x = 7$, $N_z = 5$, the cavities have dimensions down to $(\lambda/17.5)^2$ and $(\lambda/12) \times (\lambda/17)$, respectively.

The near-field microwave photonic mode plays an important role from long-distance communications to quantum interactions. With the development of on-chip miniaturized microwave photonic devices, the realization of subwavelength optical mode localization becomes a very important scientific problem. The technologies require the miniaturization of cavities, which usually leads to a decrease in the quality factor. Therefore, it is very important and meaningful to evaluate the Q/V relation in

practical applications, where Q and V correspond to the quality factor and mode volume (the length is normalized to wavelength), respectively. For example, in the field of sensors, the cavity is usually required to have high Q and small V to increase the sensitivity of the sensor [66]. In addition, there are the same requirements in microwave resonance imaging [67] and miniaturized narrowband filters [68]. However, for the usual resonant structure, the value of Q of the cavity mode tends to decrease with a decrease in V. Fortunately, the miniaturized high-Q cavity mode in the hyperbolic cavity provides a good solution for the realization of large Q/V. In Fig. 7(c), for $N_z = 5$, the Q/V values of the C_{11} cavity mode in the hyperbolic cavities with $N_x = 5$ and $N_x = 7$ are 524.71 and 438.61, respectively. The Q/V value of the cavity mode can be effectively increased when the structure size is reduced in the x direction. Similarly, in Fig. 7(d), for $N_x = 7$, the Q/V values of the C_{11} cavity mode in the hyperbolic cavities with $N_z = 1$, $N_z = 3$, and $N_z = 5$ are 1822.73, 481.29, and 438.61, respectively. The Q/V value of the

cavity mode can also be effectively increased when the structure's size is reduced in the z direction. In addition, in Fig. 7(e), the Q/V values of the C_{11} cavity mode in the hyperbolic cavities with $N_x = 4$, $N_x = 4$ and $N_x = 7$, $N_z = 5$ are 1691.63 and 438.61, respectively. It is further determined that Q/V can be effectively increased by reducing the size of the hyperbolic cavity. Hence, the experimental realization of magnetic hyperbolic cavities on a planar circuit-based metamaterial offers great practical advantages in the technology and potential microwave applications, such as high-sensitivity sensors, resonance imaging, and miniaturized narrowband filters. In addition, the proposed circuit-based hyperbolic cavities give important potential to accelerate the development of highly integrated functional devices and circuits in the microwave regime.

To end this section, experimental work demonstrating the ASL of the circuit-based magnetic hyperbolic cavity is discussed. The sample (same as that schematically illustrated in Fig. 1) and a schematic of the near-field detection system are shown in Fig. 8(a). The size of the circuit-based hyperbolic is $N_x = 7$, $N_z = 5$. In the experimental process, signals are generated from a vector network analyzer (Agilent PNA Network Analyzer N5222A). A subminiature version A (SMA) connector that functions as the source for the system is placed at the center of the sample as a vertical monopole to excite the circuit-based prototype. A small homemade rod antenna of 2 mm is employed to measure the out-of-plane electric field E_y at a fixed height of 1 mm from the planar microstrip. The measured normalized E_y spectrum for the hyperbolic cavity is shown in Fig. 8(b). In a certain frequency region, four cavity modes can be seen and they are all marked based on the mode order. The corresponding electric field E_y distributions are shown in Figs. 8(c)–8(f). In our experiments, the sample is placed on an automatic translation device that makes it feasible and accurate to probe the field distribution through near-field scanning measurements. The spatial steps for near-field scanning are set at 1 mm in the x and y directions. The field amplitudes are normalized according to their respective maximum amplitude. The measured field distributions of the cavity modes C_{71}, C_{51}, C_{31}, and C_{11} in Figs. 8(c)–8(f), respectively, show that the higher order mode is found at a lower resonant frequency, which agrees well with the simulation results in Fig. 5. Therefore, the anomalous mode-order property of the hyperbolic cavity in the x direction is experimentally demonstrated in the circuit-based system.

IV. NEAR-FIELD COUPLING BETWEEN TWO HYPERBOLIC CAVITIES

Recently, technology has required the miniaturization of cavities, and this usually leads to a decrease in Q. Specifically, an alternative way to confine subwavelength light with high Q is to use destructive interference in the regime
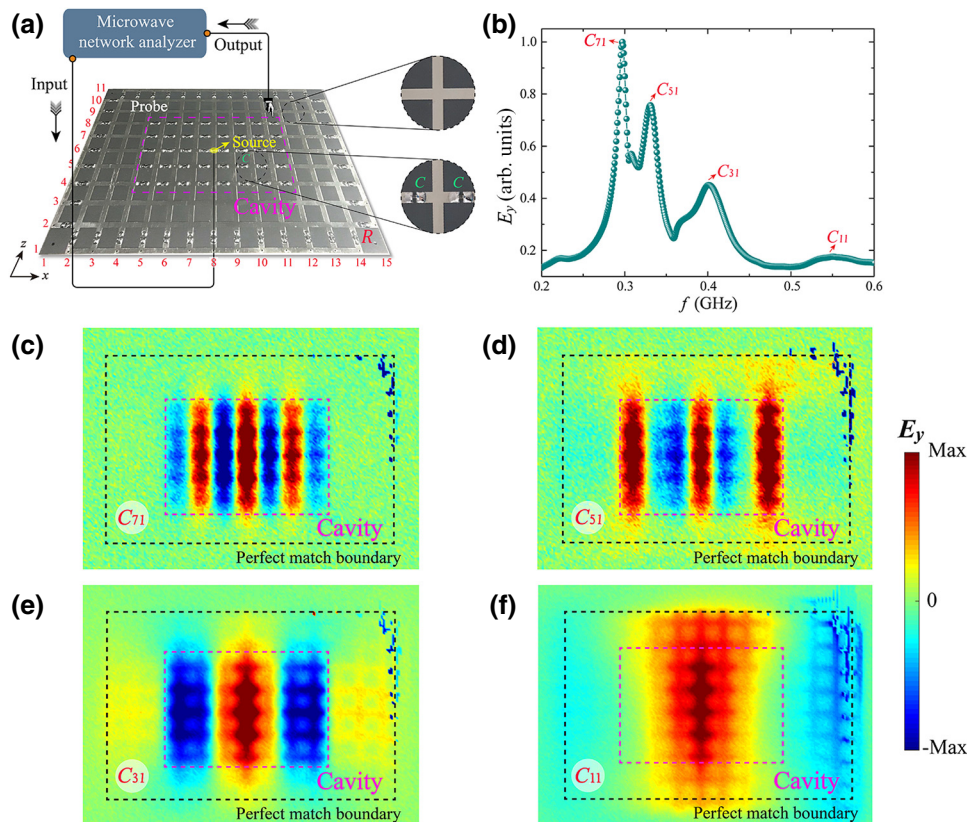

FIG. 8. (a) Experimental schematic of the TL-based hyperbolic cavity. Insets show the amplified real structure photos of HMM and background medium, respectively. (b) Measured normalized E_y spectra for the hyperbolic cavity modes. (c)–(f) Measured near-field distributions of E_y at four different frequencies: (c) 0.295 GHz (order C_{71}), (d) 0.331 GHz (order C_{51}), (e) 0.401 GHz (order C_{31}), and (f) 0.550 GHz (order C_{11}). Order number for each case is shown at the lower left of each part.

of bound states in the continuum (BIC) [69,70]. This mechanism is the result of the destructive interference between two modes of the same cavity, which is mainly implemented using high-index all-dielectric structures [69,70]. Here, we use the destructive interference between two hyperbolic cavity modes to provide a completely different approach, with the same the goals, to create simultaneously a subwavelength and high-Q cavity. With the assistance of the high-k modes, the hyperbolic cavity can overcome the size limitations of the traditional cavity [34,35]. The ultrasmall hyperbolic cavity can be used as a meta-atom, which may be useful to study many interesting fields of physics, such as the classical analogy of quantum optics [71], non-Hermitian optics [72], and topological photonics [73] in the near-field regime. In this section, the fundamental near-field coupling between two hyperbolic cavities is studied. The model of a metamolecule constructed from two hyperbolic cavities is shown in Fig. 9(a), where the

near-field coupling between the two cavity modes results in frequency splitting. The size of each hyperbolic cavity used in the section is $N_x = 7$, $N_z = 1$. In Fig. 9(b), the two hyperbolic cavities are marked as cavity 1 and cavity 2. Because the loaded lumped capacitors in the two cavities are identical, $C_1 = C_2 = 5$ pF, the frequencies of the cavity modes in the two hyperbolic cavities are the same. The excitation source is placed at the center of cavity 1, which can be directly excited. After cavity 1 is excited, it can interact with cavity 2. The E_y spectra for cavity 1 alone and the composite structure with the two cavities are shown in Fig. 9(c). From the black dashed line, we can see cavity mode C_{71} (0.7188 GHz) for cavity 1. When the two hyperbolic cavities are coupled, an EIT-like spectrum with an EIT window of about $f_0' = 0.7176$ GHz appears. The EIT-like spectrum originates from the interference between the two identical hyperbolic cavities. The two typical splitting peaks at lower and higher frequencies correspond to
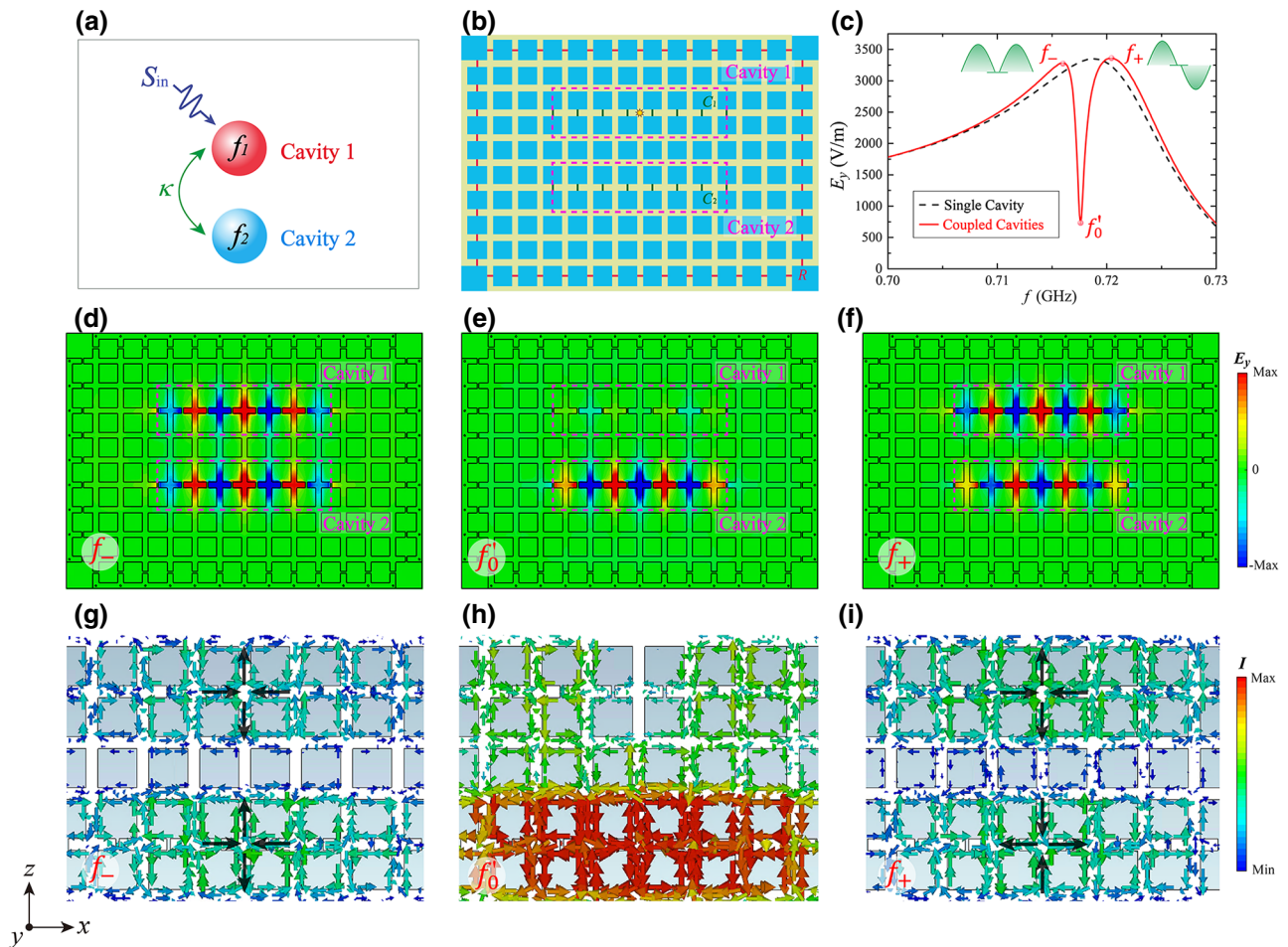

FIG. 9. (a) Model of metamolecule constructed by two hyperbolic cavities. (b) Schematic of the TL-based structure with two hyperbolic cavities of the same size $N_x = 7$, $N_z = 1$ and $C_1 = C_2 = 5$ pF. (c) Simulated E_y spectra for the single hyperbolic cavity with $N_x = 7$, $N_z = 1$ and the coupled structure in (b). Interaction between the two cavity modes leads to bonding and antibonding modes in the whole coupled structure. (d)–(f) Simulated E_y spectra of the structure in (b) at three typical frequencies of the EIT spectrum. (g)–(i) Corresponding surface current density distributions. Black lines (arrows) indicate the directions at the center of the cavities.
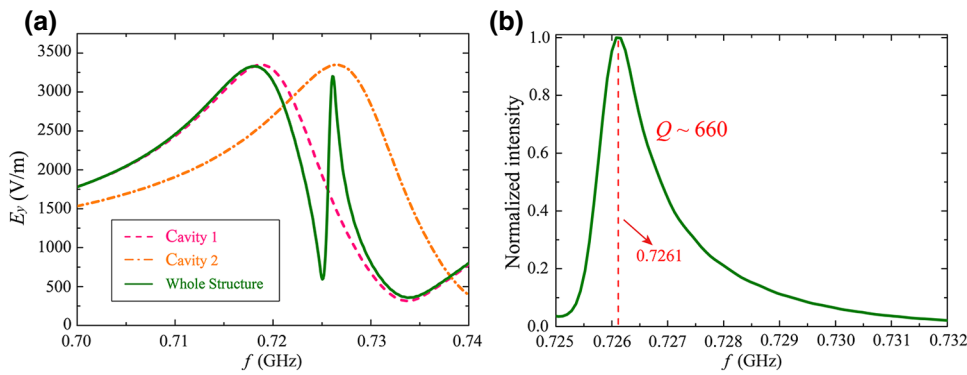
FIG. 10. (a) Simulated E_y spectra of cavity 1 (pink dashed line), cavity 2 (orange dot dash line), and the whole structure (green solid line). Two cavities of the same size $N_x = 7$, $N_z = 1$. However, there is a small detuning of the lumped capacitor for the two hyperbolic cavities $C_1 = 5$ pF, $C_2 = 4.89$ pF. (b) Magnification of the curve of the normalized narrow peak in (a).

$f_- = 0.7159$ GHz and $f_+ = 0.7204$ GHz, respectively. For the two peaks in the spectrum, it can be seen that the local fields are concentrated inside the two cavities in Figs. 9(d) and 9(f). In particular, the bonding and antibonding modes are formed at f_- and f_+, which are shown in Figs. 9(d) and 9(f). From the dip in the spectrum, it is clear that cavity 1 is weakly excited and the local field is mainly concentrated inside cavity 2, as shown in Fig. 9(e). Figures 9(g)–9(f) indicate the corresponding surface current density of modes at f_-, f_0', and f_+. The directions of the surface current show that the bonding and antibonding modes form at f_- and f_+. Black lines (arrows) indicate the directions at the center of the cavities.

As mentioned above, an EIT-like response arises in the composite structure with two identical hyperbolic cavities. If the loaded capacitors in cavity 2 are changed to $C_2 = 4.89$ pF, the frequency of cavity mode C_{71} in cavity 2 changes to 0.7265 GHz. The individual E_y spectra of single cavity 1 and single cavity 2 are marked by the pink dashed line and orange dotted-dashed line in Fig. 10(a), respectively. For the composite structure with two hyperbolic cavities, their corresponding modes couple with each other and the symmetry of the spectrum will be broken, which is marked by the solid green line in Fig. 10(a). It is the interference of the above two cavity modes with different frequencies that generates the Fano resonance [71,74]. Therefore, the spectrum of the Fano resonance experiences a large change over a very narrow frequency range because of the destructive interference between the two hyperbolic cavity modes. The Q factor of the sharp resonance is extracted from the intensity spectrum as 660 in Fig. 10(b).

V. CONCLUSION

A circuit-based magnetic HMM based on the TL system is set up in this work. Based on the planar structure, the abnormal resonant property is experimentally observed to be associated with the frequency, direction, and size; this agrees with the theoretical predictions that the scaling laws are anisotropic for different directions in the hyperbolic cavities. An effective hyperbolic cavity is experimentally fabricated and an ASL in the x direction is demonstrated.

Moreover, this ultrasmall hyperbolic cavity is used to control the spectral response based on near-field coupling. The results for the circuit-based magnetic hyperbolic cavity not only provide a good platform to study physical phenomena, such as ASLs, but may also be very useful in various applications in planar integrated microwave photonics, such as high-sensitivity sensors, resonance imaging, and miniaturized narrowband filters.

[1] A. Poddubny, I. Iorsh, P. Belov, and Y. Kivshar, Hyperbolic metamaterials, Nat. Photon. **7**, 948 (2013).

[2] V. P. Drachev, V. A. Podolskiy, and A. V. Kildishev, Hyperbolic metamaterials: New physics behind a classical problem, Opt. Express **21**, 15048 (2013).

[3] P. Shekhar, J. Atkinson, and Z. Jacob, Hyperbolic metamaterials: Fundamentals and applications, Nano Converg **1**, 14 (2014).

[4] L. Ferrari, C. H. Wu, D. Lepage, X. Zhang, and Z. W. Liu, Hyperbolic metamaterials and their applications, Prog. Quantum Electron. **40**, 1 (2015).

[5] I. I. Smolyaninov, *Hyperbolic Metamaterials* (Morgan & Claypool / Institute of Physics, London, 2018).

[6] Z. W. Guo, H. T. Jiang, and H. Chen, Hyperbolic metamaterials: From dispersion manipulation to applications, J. Appl. Phys. **127**, 071101 (2020).

[7] A. A. High, R. C. Devlin, A. Dibos, M. Polking, D. S. Wild, J. Perczel, N. P. de Leon, M. D. Lukin, and H. Park, Visible-frequency hyperbolic metasurface, Nature **522**, 192 (2015).

[8] R. Z. Zhang and Z. M. Zhang, Tunable positive and negative refraction of infrared radiation in graphene dielectric multilayers, Appl. Phys. Lett. **107**, 191112 (2015).

[9] P. X. Zheng, Q. Xu, X. Q. Su, D. Y. Wang, Y. H. Xu, X. Q. Zhang, Y. F. Li, Z. Tian, J. Q. Gu, L. Y. Liu, C. M. Ouyang, J. G. Han, and W. L. Zhang, Anomalous wave propagation in topological transition metasurfaces, Adv. Opt. Mater. **7,** 1801483 (2019).

[10] K. Yu, Z. W. Guo, H. T. Jiang, and H. Chen, Loss-induced topological transition of dispersion in metamaterials, J. Appl. Phys. **119,** 203102 (2016).

[11] Z. W. Guo, H. T. Jiang, Y. Sun, Y. H. Li, and H. Chen, Actively controlling the topological transition of dispersion based on electrically controllable metamaterials, Appl. Sci. **8,** 596 (2018).

[12] Z. W. Guo, H. T. Jiang, K. J. Zhu, Y. Sun, Y. H. Li, and H. Chen, Focusing and Super-Resolution with Partial Cloaking Based on Linear-Crossing Metamaterials, Phys. Rev. Appl. **10,** 064048 (2018).

[13] X. Yin, H. Zhu, H. J. Guo, M. Deng, T. Xu, Z. J. Gong, X. Li, Z. H. Hang, C. Wu, H. Q. Li, S. Q. Chen, L. Zhou, and L. Chen, Hyperbolic metamaterial devices for wavefront manipulation, Laser Photon. Rev. **13,** 1800081 (2019).

[14] Z. W. Guo, H. T. Jiang, and H. Chen, Linear-crossing metamaterials mimicked by multi-layers with two kinds of single negative materials, J. Phys: Photon. **2,** 011001 (2020).

[15] H. Shen, D. Lu, B. VanSaders, J. J. Kan, H. X. Xu, E. E. Fullerton, and Z. W. Liu, Anomalously Weak Scattering in Metal-Semiconductor Multilayer Hyperbolic Metamaterials, Phys. Rev. X. **5,** 021021 (2015).

[16] C. Qian, X. Lin, Y. Yang, F. Gao, Y. C. Shen, J. Lopez, I. Kaminer, B. L. Zhang, E. P. Li, M. Soljačić, and H. S. Chen, Multifrequency superscattering from subwavelength hyperbolic structures, ACS Photon. **5,** 1506 (2018).

[17] I. I. Smolyaninov and E. E. Narimanov, Metric Signature Transitions in Optical Metamaterials, Phys. Rev. Lett. **105,** 067402 (2010).

[18] H. N. Krishnamoorthy, Z. Jacob, E. Narimanov, I. Kretzschmar, and V. M. Menon, Topological transitions in metamaterials, Science **336,** 205 (2012).

[19] I. I. Smolyaninov, Y.-J. Hung, and C. C. Davis, Magnifying superlens in the visible frequency range, Science **315,** 1699 (2007).

[20] Z. W. Liu, H. Lee, Y. Xiong, C. Sun, and X. Zhang, Far-field optical hyperlens magnifying sub-diffraction-limited objects, Science **315,** 1686 (2007).

[21] B. D. F. Casse, W. T. Lu, Y. J. Huang, E. Gultepe, L. Menon, and S. Sridhar, Super-resolution imaging using a three-dimensional metamaterials nanolens, Appl. Phys. Lett. **96,** 023114 (2010).

[22] K. V. Sreekanth, Y. Alapan, M. ElKabbash, E. Ilker, M. Hinczewski, U. A. Gurkan, A. De Luca, and G. Strangi, Extreme sensitivity biosensing platform based on hyperbolic metamaterials, Nat. Mater. **15,** 621 (2016).

[23] E. Shkondin, T. Repän, M. E. Aryaee Panah, A. V. Lavrinenko, and O. Takayama, High aspect ratio plasmonic nanotrench structures with large active surface area for label-free mid-infrared molecular absorption sensing, ACS Appl. Nano Mater. **1,** 1212 (2018).

[24] I. I. Smolyaninov, Giant Unruh effect in hyperbolic metamaterial waveguides, Opt. Lett. **44,** 2224 (2019).

[25] Z. Y. Huang, T. B. Norris, and E. Narimanov, Nanoscale fingerprinting with hyperbolic metamaterials, APL Photon. **4,** 026103 (2019).

[26] S.-A. Biehs, V. M. Menon, and G. S. Agarwal, Long-range dipole-dipole interaction and anomalous Förster energy transfer across a hyperbolic metamaterial, Phys. Rev. B **93,** 245439 (2016).

[27] C. L. Cortes and Z. Jacob, Super-Coulombic atom–atom interactions in hyperbolic media, Nat. Commun. **8,** 14144 (2017).

[28] R. Deshmukh, S–A Biehs, E. Khwaja, T. Galfsky, G. S. Agarwal, and V. M. Menon, Long-range resonant energy transfer using optical topological transitions in metamaterials, ACS Photon. **5,** 2737 (2018).

[29] W. D. Newman, C. L. Cortes, A. Afshar, K. Cadien, A. Meldrum, R. Fedosejevs, and Z. Jacob, Observation of long-range dipole-dipole interactions in hyperbolic metamaterials, Sci. Adv. **4,** eaar5278 (2018).

[30] Z. W. Guo, H. T. Jiang, Y. H. Li, H. Chen, and G. S. Agarwal, Enhancement of electromagnetically induced transparency in metamaterials using long range coupling mediated by a hyperbolic material, Opt. Express **26,** 627 (2018).

[31] Y. R. He, S. L. He, and X. D. Yang, Optical field enhancement in nanoscale slot waveguides of hyperbolic metamaterials, Opt. Lett. **37,** 2907 (2012).

[32] S. Ishii, M. Y. Shalaginov, V. E. Babicheva, A. Boltasseva, and A. V. Kildishev, Plasmonic waveguides cladded by hyperbolic metamaterials, Opt. Lett. **39,** 4663 (2014).

[33] N. Vasilantonakis, M. E. Nasir, W. Dickson, G. A. Wurtz, and A. V. Zayats, Bulk plasmon-polaritons in hyperbolic nanorod metamaterial waveguides, Laser Photon. Rev. **9,** 345 (2015).

[34] J. Yao, X. D. Yang, X. B. Yin, G. Bartal, and X. Zhang, Three-dimensional nanometer-scale optical cavities of indefinite medium, Proc. Natl. Acad. Sci. U.S.A. **108,** 11327 (2011).

[35] X. D. Yang, J. Yao, J. Rho, X. B. Yin, and X. Zhang, Experimental realization of three-dimensional indefinite cavities at the nanoscale with anomalous scaling laws, Nat. Photon. **6,** 450 (2012).

[36] E. Travkin, T. Kiel, S. Sadofev, K. Busch, O. Benson, and S. Kalusniak, Anomalous resonances of an optical microcavity with a hyperbolic metamaterial core, Phys. Rev. B **97,** 195133 (2018).

[37] W. Wang, X. D. Yang, and J. Gao, Scaling law of Purcell factor in hyperbolic metamaterial cavities with dipole excitation, Opt. Lett. **44,** 471 (2019).

[38] C. W. Wu, A. Salandrino, X. J. Ni, and X. Zhang, Electrodynamical Light Trapping Using Whispering-Gallery Resonances in Hyperbolic Cavities, Phys. Rev. X. **4,** 021015 (2014).

[39] M. J. Wan, P. Gu, W. Y. Liu, Z. Chen, and Z. L. Wang, Low threshold spaser based on deep-subwavelength spherical hyperbolic metamaterial cavities, Appl. Phys. Lett. **110,** 031103 (2017).

[40] S. W. Tang, Y. F. Fang, L. Zhou, Z. W. Liu, and Y. F. Mei, Anomalous scaling laws of hyperbolic metamaterials in a tubular geometry, J. Opt. Soc. Am. B **35,** 391 (2018).

[41] S. R. K. C. Indukuri, J. Bar-David, N. Mazurski, and U. Levy, Ultrasmall mode volume hyperbolic nanocavities for

enhanced light−matter interaction at the nanoscale, ACS Nano **13**, 11770 (2019).

[42] Y. Cheng, C. T. Liao, Z. H. Xie, Y. C. Huang, and M. C. Lee, Study of cavity-enhanced dipole emission on a hyperbolic metamaterial slab, J. Opt. Soc. Am. B **36**, 426 (2019).

[43] K. Feng, G. Harden, D. L. Sivco, and A. J. Hoffman, Subdiffraction confinement in all-semiconductor hyperbolic metamaterial resonators, ACS Photon. **4**, 1621 (2017).

[44] K. C. Shen, C. T. Ku, C. Hsieh, H. C. Kuo, Y. J. Cheng, and D. P. Tsa, Deep-ultraviolet hyperbolic metacavity laser, Adv. Mat. **30**, 1706918 (2018).

[45] R. Sohr, D. Wei, S. Tomasulo, M. K. Yakes, and S. Law, Simultaneous large mode index and high quality factor in infrared hyperbolic metamaterials, ACS Photon. **5**, 4003 (2018).

[46] S. S. Kruk, Z. J. Wong, E. Pshenay-Severin, K. O'Brien, D. N. Neshev, Y. S. Kivshar, and X. Zhang, Magnetic hyperbolic optical metamaterials, Nat. Commun. **7**, 11329 (2016).

[47] J. S. Gomez-Diaz, M. Tymchenko, and A. Alù, Hyperbolic Plasmons and Topological Transitions Over Uniaxial Metasurfaces, Phys. Rev. Lett. **114**, 233901 (2015).

[48] O. Y. Yermakov, A. I. Ovcharenko, M. Song, A. A. Bogdanov, I. V. Iorsh, and Y. S. Kivshar, Hybrid waves localized at hyperbolic metasurfaces, Phys. Rev. B **91**, 235423 (2015).

[49] J. S. Gomez-Diaz and A. Alù, Flatland optics with hyperbolic metasurfaces, ACS Photon. **3**, 2211 (2016).

[50] Y. H. Yang, L. Q. Jing, L. Shen, Z. J. Wang, B. Zheng, H. P. Wang, E. P. Li, N. H. Shen, T. Koschny, C. M. Soukoulis, and H. S. Chen, Hyperbolic spoof plasmonic metasurfaces, NPG Asia Mater. **9**, e428 (2017).

[51] Y. H. Yang, P. F. Qin, B. Zheng, L. Shen, H. P. Wang, Z. J. Wang, E. P. Li, R. Singh, and H. S. Chen, Magnetic hyperbolic metasurface: Concept, design, and applications, Adv. Sci. **5**, 1801495 (2018).

[52] C. Hu, Z. Li, R. Tong, X. Wu, Z. Xia, L. Wang, S. Li, Y. Huang, S. Wang, B. Hou, C. T. Chan, and W. Wen, Type-II Dirac Photons at Metasurfaces, Phys. Rev. Lett. **121**, 024301 (2018).

[53] P. Huo, S. Zhang, Y. Liang, Y. Lu, and T. Xu, Hyperbolic metamaterials and metasurfaces: Fundamentals and applications, Adv. Opt. Mater. **7**, 1801616 (2019).

[54] F. Vaianella and B. Maes, Fano resonance engineering in slanted cavities with hyperbolic metamaterials, Phys. Rev. B **94**, 125442 (2016).

[55] D. Mukhopadhyay and G. S. Agarwal, Multiple Fano interferences due to waveguide-mediated phase coupling between atoms, Phys. Rev. A **100**, 013812 (2019).

[56] G. V. Eleftheriades, A. K. Iyer, and P. C. Kremer, Planar negative refractive index media using periodically LC loaded transmission lines, IEEE Trans. Microwave Theory Tech. **50**, 2702 (2002).

[57] C. Caloz and T. Itoh, *Electromagnetic Metamaterials Transmission Line Theory and Microwave Applications* (Wiley, New York, 2006).

[58] A. V. Chshelokova, P. V. Kapitanova, A. N. Poddubny, D. S. Filonov, A. P. Slobozhanyuk, Y. S. Kivshar, and P. A. Belov, Hyperbolic transmission-line metamaterials, J. Appl. Phys. **112**, 073116 (2012).

[59] A. V. Shchelokova, D. S. Filonov, P. V. Kapitanova, and P. A. Belov, Magnetic topological transition in transmission line metamaterials, Phys. Rev. B **90**, 115155 (2014).

[60] P. V. Kapitanova, P. Ginzburg, F. J. Rodríguez-Fortuño, D. S. Filonov, P. M. Voroshilov, P. A. Belov, A. N. Poddubny, Y. S. Kivshar, G. A. Wurtz, and A. V. Zayats, Photonic spin Hall effect in hyperbolic metamaterials for polarization-controlled routing of subwavelength modes, Nat. Commun. **5**, 3226 (2014).

[61] C. R. Simovski, P. A. Belov, A. V. Atrashchenko, and Y. S. Kivshar, Wire metamaterials: Physics and applications, Adv. Mater. **24**, 4229 (2012).

[62] O. Y. Yermakov, A. A. Hurshkainen, D. A. Dobrykh, P. V. Kapitanova, I. V. Iorsh, S. B. Glybovski, and A. A. Bogdanov, Experimental observation of hybrid TE-TM polarized surface waves supported by a hyperbolic metasurface, Phys. Rev. B **98**, 195404 (2018).

[63] Z. W. Guo, H. T. Jiang, Y. Long, K. Yu, J. Ren, C. H. Xue, and H. Chen, Photonic spin Hall effect in waveguides composed of two types of single-negative metamaterials, Sci. Rep. **7**, 7742 (2017).

[64] J. Ran, Y. W. Zhang, X. D. Chen, and H. Chen, Frequency mixer based on Doppler effect, IEEE Microw. Wireless Compon. Lett. **28**, 43 (2017).

[65] Y. Li, Y. Sun, W. W. Zhu, Z. W. Guo, J. Jiang, T. Kariyado, H. Chen, and X. Hu, Topological LC-circuits based on microstrips and observation of electromagnetic modes with orbital angular momentum, Nat. Commun. **9**, 4598 (2018).

[66] X. P. Shen and T. J. Cui, Ultrathin plasmonic metamaterial for spoof localized surface plasmons, Laser Photonics Rev. **8**, 137 (2014).

[67] A. P. Slobozhanyuk, A. N. Poddubny, A. J. E. Raaijmakers, C. A. T. van den Berg, A. V. Kozachenko, I. A. Dubrovina, I. V. Melchakova, Y. S. Kivshar, and P. A. Belov, Enhancement of magnetic resonance imaging with metasurfaces, Adv. Mat. **28**, 1832 (2016).

[68] P. Jarry and J. Beneat, *Design and Realizations of Miniaturized Fractal Microwave and RF Filters* (John Wiley & Sons, New York, 2009).

[69] C. W. Hsu, B. Zhen, A. D. Stone, J. D. Joannopoulos, and M. Soljačić, Bound states in the continuum, Nat. Rev. Mater. **1**, 1 (2016).

[70] A. Kodigala, T. Lepetit, Q. Gu, B. Bahari, Y. Fainman, and B. Kanté, Lasing action from photonic bound states in continuum, Nature **541**, 196 (2017).

[71] B. Luk'yanchuk, N. I. Zheludev, S. A. Maier, N. J. Halas, P. Nordlander, H. Giessen, and C. T. Chong, The Fano resonance in plasmonic nanostructures and metamaterials, Nat. Mater. **9**, 707 (2010).

[72] R. El-Ganainy, K. G. Makris, M. Khajavikhan, Z. H. Musslimani, S. Rotter, and D. N. Christodoulides, Non-Hermitian physics and PT symmetry, Nat. Phys. **14**, 11 (2018).

[73] T. Ozawa, H. M. Price, A. Amo, N. Goldman, M. Hafezi, L. Lu, M. C. Rechtsman, D. Schuster, J. Simon, O. Zilberberg, and I. Carusotto, Topological photonics, Rev. Mod. Phys. **91**, 015006 (2019).

[74] W. Q. Cai, Y. C. Fan, X. C. Huang, Q. H. Fu, R. S. Yang, W. Zhu, and F. L. Zhang, Electromagnetically induced transparency in all-dielectric metamaterials: Coupling between magnetic Mie resonance and substrate resonance, Phys. Rev. A **100**, 053804 (2019).